Computers and Concrete, Vol. 1, No. 3 (2004) 261-284
DOI: http://dx.doi.org/10.12989/cac.2004.1.3.261

Three dimensional finite element simulations of fracture tests using the Craft concrete model

A. D. Jefferson†, B. I. G. Barr‡, T. Bennett‡† and S. C. Hee‡‡

Cardiff University, School of Engineering, P O. Box 925, Cardiff CF24 0YF, U.K.
(Received December 20, 2003, Accepted June 17, 2004)

Abstract. Two enhancements to a recently developed plastic-damage-contact model for concrete are presented. The model itself, which uses planes of degradation that can undergo damage and separation but that can regain contact according to a contact law, is described. The first enhancement is a new damage evolution function which provides a completely smooth transition from the undamaged to the damaged state and from pre-peak to post-peak regions. The second is an improved contact function that governs the potential degree of contact with increasing opening on a crack plane. The use of a damage evolution function with a pre-peak has implications for the consistent tangent matrix/stress recovery algorithm developed for the model implementation, and amendments to this algorithm to accommodate the new function are described. A series of unpublished experimental tests on notched specimens undertaken in Cardiff in the mid 1990s are then described. These include notched beam tests as well as prismatic and cylindrical torsion tests. The tests are then considered in three dimensional finite element analyses using the modified Craft model implemented in the finite element program LUSAS. Comparisons between experimental and numerical data show reasonable agreement except that the numerical simulations do not fully describe the latter stages of the softening responses for the torsion examples. Finally, it is concluded that the torsion tests described provide useful benchmark examples for the validation of three-dimensional numerical models for concrete.

Keywords: finite element; concrete; fracture; damage; plasticity; fracture tests; constitutive; contact.

1. Introduction

The numerical simulation of concrete fracture, at both micro and macro levels, is a subject that has received much attention in recent years. Work in this area has progressed on many fronts. There have been significant developments in the field of constitutive modelling, which includes the development of models based on plasticity theory (Este and Willam 1994, Grassl, *et al.* 2002), damage theory (Krajcinovic 1996, Luccioni and Oller 2003), plastic-damage theory (Lubliner, *et al.* 1989, Meshke, *et al.* 1998) and the micro-plane theory (Bažant, *et al.* 2000, Ozbolt and Reinhardt 2002). Much work has been undertaken recently on numerical techniques for capturing strong discontinuities using finite element meshes, and this has included the development of elements with embedded localisation bands (Oliver, *et al.* 2003, Mosler and Meschke 2003) as well as the so-called

† Senior Lecturer
‡ Professor
‡† Research Associate
‡‡ Research Student

partition of unity approach in which nodes of finite element meshes are enriched to allow the simulation of cracks across meshes (Wells and Sluys 2001, Moes and Belytschko 2002, de Borst 2003).

A review of examples used in the above references suggests that there is a genuine shortage of data suitable for validating three-dimensional models for concrete fracture. In the present paper this issue is addressed and a number of analyses are presented that are based on a series of torsion tests undertaken at Cardiff University in the U.K. by Barr and Brokenshire (1996), Brokenshire (1995). Whilst the test geometry has been described in Barr and Brokenshire (1996), full details of the tests have not been reported in the literature and therefore a relatively full description is provided in this contribution.

The finite element (F.E.) analyses presented here were carried out using the program LUSAS (2003) in which the Craft plastic-damage-contact concrete model, recently developed by the first author, has been implemented (Jefferson 2003a,b). This model uses embedded planes of degradation that can undergo damage and separation but that can regain contact according to a contact law. The damage-contact and plasticity components have been integrated into a single model using a thermodynamically consistent framework. The present paper provides an overview of Craft and discusses two enhancements to the model. The first of these is a pre-peak/post-peak damage evolution function which provides a smooth transition from the undamaged to damaged state and from the pre-peak to post-peak regions. It also allows separate scaling of the pre and post-peak sections, which is important because in the pre-peak stage, the function is governed by a material strain parameter, whereas in the post-peak stage the main strain parameter depends upon a characteristic length which, in a finite element context, varies with element size. The use of this approach requires a significant modification to the implicit stress recovery consistent tangent matrix algorithm. The second enhancement is a new contact potential function, which governs the proportion of damaged material within a representative volume that can regain contact with only shear displacement. This new function is smooth with respect to the opening displacement parameter. Overall it has been found that the use of damage and contact functions, that give smooth transitions between damaged and contact states, improves the convergence properties of the model and allowed the torsion tests considered in this contribution to be simulated.

The aims of the paper are therefore to

(i) present developments to the Craft model,

(ii) present experimental data, not previously published, suitable for validating three dimensional finite elements for concrete cracking and

(iii) present comparisons between these data and numerical results to validate the Craft model.

2. Craft model theory

One of the key aims in developing the Craft model was that it should be able to simulate directional cracking, crack closure and shear contact (or aggregate interlock) behaviour in an integrated manner, which also accounted for the type of damage and triaxial frictional response that characterises the behaviour of concrete in compression. A further aim was that the model should be based upon a thermodynamically consistent framework. It was concluded that in order to achieve this, the model would need to have directional damage planes that at some point in a loading process become fixed in direction. However, a problem in deriving a model that predicts directional damage is how to simulate complete loss of strength in one direction whilst maintaining strength in

other directions. These difficulties are well known but they are summarised here since describing them helps to provide the rationale behind the model. If a strain based damage surface is used with a kinematic constraint, then damage will continue to be predicted even if a macro crack has completely opened. Conversely the problem with a stress based damage surface is that the surface shrinks to zero size in stress space with complete damage, resulting in undefined gradients; furthermore, it is not easy to decide upon what local strains the transformed stresses should be linked to. It is possible to base a model on a total principal strain crack criterion but a simple example shows the difficulty of this approach. In uniaxial compression such an approach predicts cracks in directions normal to loading and whilst this is reasonable because cross-cracking does occur, there is a difficulty in that it is associated with zero stress in that direction, and it is not easy to maintain such a zero stress condition in a strain based formulation. Some long-standing models provide solutions to some of these problems, for example Ortiz (1985), however they do not address the problem of how to correctly simulate the shear behaviour of formed macro cracks or fully three-dimensional behaviour.

The above problem of strain based damage models continuing to predict further damage when a directional crack has fully formed has been addressed in recent work on strong discontinuities. For example Oliver, *et al.* (2002) present details of a method for simulating the transition from distributed damage to a strong discontinuity using a scalar damage model as a basis. The present model has not been implemented with a strong discontinuity approach, but it is compatible with such an approach, although some work would be required to achieve such an implementation.

The difficulty of how to define a local stress-strain law and integrate it with a generalised model for concrete in a thermodynamically valid manner is almost certainly one of the reasons that developments of the once favoured plastic cracking models (Owen, *et al.* 1983, de Borst and Nauta 1985) has largely ceased.

Most existing large finite element codes have material model interfaces that make the inclusion of a new material model relatively straight-forward. It is thus still an attractive prospect to have a model that is able to reasonably predict the main characteristics of concrete behaviour at the material level only. However, it acknowledged that such an approach will always be limited because the constraints provided by standard elements will not ever correctly predict strong discontinuities fully (Mosler and Meschke 2003).

Some of the difficulties relating to concrete material modelling, discussed above, were addressed in the development of the Craft model. In this model embedded damage-contact planes were integrated with a plasticity component by using a thermodynamically consistent plastic-damage framework. The essential elements of the model are

- A local stress strain relationship, which here is a damage-contact model
- A function from which local strains can be computed such that the local and global constitutive relationships are both satisfied. This is termed the total-local function.
- A triaxial plasticity component for simulating frictional behaviour and strength increase with triaxial confinement
- A thermodynamically consistent global stress-strain relationship

The model has been developed with an implicit stress recovery consistent tangent matrix algorithm, which is described in full in Jefferson (2003b). Here only the main governing relationships relevant to the present applications will be provided.

2.1. Local stress-strain relationship

The local stress comprises two components, the undamaged component and the damaged contact component, with the former being associated with the proportion of material that is undamaged $(1-\omega)$ and the latter the proportion that is damaged ω, with ω being a damage variable that lies in the range 0 to 1. The local stress is then as follows

$$\mathbf{s}_i = [(1-\omega_i)\mathbf{D}_L\mathbf{e}_i] + [H_f(\mathbf{e})\omega_i\mathbf{D}_L\mathbf{g}_i] = \begin{bmatrix}\text{undamaged}\\ \text{component}\end{bmatrix} + \begin{bmatrix}\text{damaged contact}\\ \text{component}\end{bmatrix} \tag{1}$$

$\mathbf{s}_i$, $\mathbf{e}_i$, $\mathbf{D}_L$ are the local stress, local effective strain and local elastic constitutive matrix respectively for damage plane i. s_1 and e_1 denote normal components and s_2, s_3 and e_2, e_3, shear components of the local stress and strain vectors respectively. H_f is a function that varies from 1 to 0 with the increasing crack opening parameter e_g, and this simulates the observed phenomena that the wider a crack is open, the less the shear that can be transferred across it. ω_i, the damage variable, depends upon a local strain parameter ζ_i. $\mathbf{g}_i$ is the strain relative to a contact surface, which is illustrated in Fig. 1. It is related by a transformation to the local strains $\mathbf{e}_i$, as follows;

$$\mathbf{g}_i = \mathbf{\Phi}_{di}\mathbf{e}_i \tag{2}$$

In the interlock region $\mathbf{\Phi}_d = \mathbf{\Phi}_g$ and takes the form given in Eq. (3)

$$\mathbf{\Phi}_g = \frac{1}{1+m_g^2}\left(\left(\frac{\partial\phi_{int}}{\partial\mathbf{e}}\right)\cdot\left(\frac{\partial\phi_{int}}{\partial\mathbf{e}}\right)^T + \phi_{int}\frac{\partial^2\phi_{int}}{\partial\mathbf{e}^2}\right) \tag{3}$$

where $\phi_{int}(\mathbf{e}) = m_g e_1 - \sqrt{e_2^2+e_3^2}$ and in which m_g is the slope of the Interlock contact surface, as shown in Fig. 1. In two dimensions this takes the form

$$\mathbf{\Phi}_g = \frac{1}{1+m_g^2}\begin{bmatrix} m_g^2 & -m_g \\ -m_g & 1\end{bmatrix} \tag{4}$$

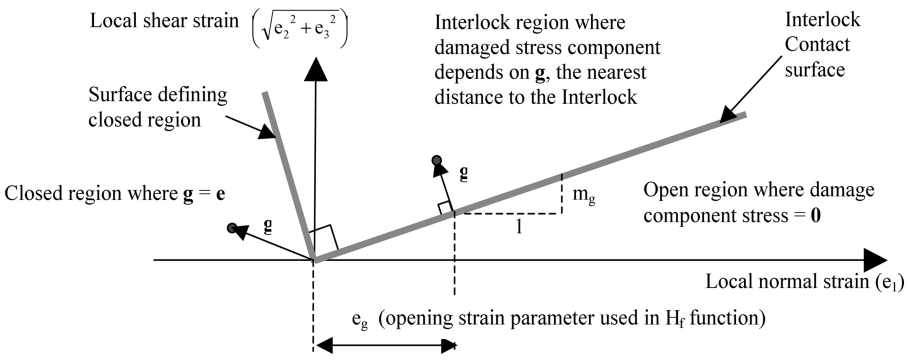

Fig. 1 Contact surface

$$\mathbf{s}_i = \mathbf{D}_L[(1-\omega_i) + H_f\omega_i\mathbf{\Phi}_d]\mathbf{e}_i = \mathbf{D}_L\mathbf{M}_{xi}\mathbf{e}_i \tag{5}$$

It is noted that in Jefferson (2003a) (1-ω) was denoted by h_c and $H_f\omega$ by h_f.

The effective local strains ($\mathbf{e}_i$) are those that apply to a fracture process zone of an effective crack plane. They are taken as equal to the relative displacements across the zone divided by the effective zone width w_c. The advantage of using $\mathbf{e}_i$ as the basis for the local model is that these local strains (or relative displacements) can be measured directly from tests. However, it is the inelastic component of these strains ($\mathbf{e}_f$) that is required in the global stress-strain relationship, but it is $\mathbf{e}$, not $\mathbf{e}_f$, that is derived from the total-local function described below and therefore $\mathbf{e}_f$ is eliminated from the global stress-strain relationship by the use of Eq. (6). The inelastic local strain vector is given by

$$\mathbf{e}_f = (\mathbf{I} - \mathbf{M}_x)\mathbf{e} \tag{6}$$

The local damage function $\phi(\mathbf{e},\zeta)$ is asymptotic to an equivalent strain friction surface and is orthogonal to the normal strain axis at its intercept with that axis, i.e., at $e_1 = \zeta$, e_2=e_3=0.

$$\phi(\mathbf{e},\zeta) = \frac{e_1}{2}\left[1 + \left(\frac{\mu_\varepsilon}{r_\zeta}\right)^2\right] + \frac{1}{2r_\zeta^2}\sqrt{(r_\zeta^2 - \mu_\varepsilon^2)^2 e_1^2 + 4r_\zeta^2(e_2^2 + e_3^2)} - \varsigma \tag{7}$$

The material constants r_ζ and μ_ε are the relative shear strain intercept and the asymptotic shear friction factor respectively. These are the strain equivalents of the relative shear stress intercept $r_\sigma = c/f_t$ and the asymptotic friction factor μ, noting that c is the shear stress intercept.

2.2. Overall stress strain relationship

The global stress-strain relationship is given by

$$\sigma = \mathbf{D}_e\left((\boldsymbol{\varepsilon} - \boldsymbol{\varepsilon}_p) - \sum_{j=1}^{n_p}\mathbf{N}_j^T(\mathbf{I} - \mathbf{M}_{x_j})\mathbf{e}_j\right) \tag{8}$$

in which $\mathbf{D}_e$ is the elastic tensor, $\boldsymbol{\sigma}$ the stress tensor, $\boldsymbol{\varepsilon}$ the strain tensor and $\boldsymbol{\varepsilon}_p$ the plastic strain tensor, and n_p = number of damage planes.

$\mathbf{N}_i$ is the stress transformation matrix such that

$$\mathbf{s}_i = \mathbf{N}_i\boldsymbol{\sigma} \tag{9}$$

where

$$\mathbf{N}_i = \begin{bmatrix} r_{d_1}^2 & r_{d_2}^2 & r_{d_3}^2 & 2r_{d_1}r_{d_2} & 2r_{d_2}r_{d_3} & 2r_{d_1}r_{d_3} \\ s_{d_1}^2 & s_{d_2}^2 & s_{d_3}^2 & 2s_{d_1}s_{d_2} & 2s_{d_2}s_{d_3} & 2s_{d_1}s_{d_3} \\ t_{d_1}^2 & t_{d_2}^2 & t_{d_3}^2 & 2t_{d_1}t_{d_2} & 2t_{d_2}t_{d_3} & 2t_{d_1}t_{d_3} \end{bmatrix}_i$$

r_{d_1}, r_{d_2}, r_{d_3} are the x,y,z components of the unit vector $\mathbf{r}_d$, normal to the POD surface and $\mathbf{s}_d$ and $\mathbf{t}_d$ are the in-plane vectors.

It is noted that in Eq. (8) the inelastic component of strain resulting from each plane of degradation is equal to the product of the strain transformation matrix and the local inelastic strain vector i.e., $\mathbf{N}_i{}^T\mathbf{e}_{fi}$

Applying transformation (9) and using Eqs. (5) and (6) the stress recoverable-strain relationship may be obtained to be;

$$\boldsymbol{\sigma} = \left(\mathbf{I} + \mathbf{D}_e \sum_{j=1}^{n_p} \mathbf{N}_j^T (\mathbf{M}_x^{-1} - \mathbf{I}) \mathbf{C}_L \mathbf{N}_j \right)^{-1} \mathbf{D}_e (\boldsymbol{\varepsilon} - \boldsymbol{\varepsilon}_p) \tag{10}$$

in which $\mathbf{C}_L = \mathbf{D}_L{}^{-1}$ and $\mathbf{I}$ denotes the identity matrix (tensor).

2.3. Total-local function

One of the key components of the model is the Total-local vector function, and it is use of this function that allows the local and global constitutive relationships, as well as the stress transformation (9), to be simultaneously satisfied for multiple damage planes. The model therefore has full coupling between damage surfaces. The function, shown below, gives the error between the transformed global stresses computed from Eq. (10) and the local stresses computed from Eq. (5). This is equated to zero and solved for the unknown local strains $\mathbf{e}_i$

$$\mathbf{f}_{e_i} = \mathbf{N}_i \boldsymbol{\sigma} - \mathbf{s}_i = \mathbf{N}_i \left[\mathbf{D}_e (\boldsymbol{\varepsilon} - \boldsymbol{\varepsilon}_p) - \sum_{j=1}^{n_p} \mathbf{N}_j^T (\mathbf{I} - \mathbf{M}_{xj}) \mathbf{e}_j \right] - \mathbf{D}_L \mathbf{M}_{xi} \mathbf{e}_i = 0 \tag{11}$$

When two planes are present Eq. (11) may be written as;

$$\begin{bmatrix} \mathbf{N}_1 \mathbf{D}_e \mathbf{N}_1^T (\mathbf{I} - \mathbf{M}_{x1}) + \mathbf{D}_L \mathbf{M}_{x1} & \mathbf{N}_1 \mathbf{D}_e \mathbf{N}_2^T (\mathbf{I} - \mathbf{M}_{x2}) \\ \mathbf{N}_2 \mathbf{D}_e \mathbf{N}_1^T (\mathbf{I} - \mathbf{M}_{x1}) & \mathbf{N}_2 \mathbf{D}_e \mathbf{N}_2^T (\mathbf{I} - \mathbf{M}_{x2}) + \mathbf{D}_L \mathbf{M}_{x2} \end{bmatrix} \begin{bmatrix} \mathbf{e}_1 \\ \mathbf{e}_2 \end{bmatrix} = \begin{bmatrix} \mathbf{N}_1 \\ \mathbf{N}_2 \end{bmatrix} \mathbf{D}_e (\boldsymbol{\varepsilon} - \boldsymbol{\varepsilon}_p) \tag{12}$$

When more than one damage plane is present, a nonlinear solution procedure is required for Eq. (11), but it has been found that very few iterations of a Newton procedure are required to achieve convergence of Eq. (11) when multiple surfaces are active.

2.4. Plasticity component

The plasticity component uses a triaxial yield function developed from the yield function used by Lubliner, *et al.* (1989) but it is rounded in the pi-plane using the well-known Willam and Warnke (1975) function. A similar function form is used for the plastic potential but a dilatancy parameter (ψ) is included that controls the slope of the straight meridians. If this parameter is set to unity the potential takes the same form as the yield function and the plastic flow is associated, whereas if it is

set to zero, the model predicts zero dilatancy. The surface changes shape according to a friction hardening/softening function that is dependent upon a plastic work parameter. The tensile apex of the yield surface is not an issue because the damage component of the model ensures the apex is never reached. Full details of the plasticity component of the model are given in Jefferson (2003a), but since this contribution focuses on developments to the damage component, the details of the plasticity functions will not be provided here.

3. Smooth pre and post peak damage evolution function

In the original Craft model a well-known single term exponential softening curve, of the form suggested by Gopalaratnam and Shah (1985), was employed for the damage evolution function. This evolution function relates the damage strain parameter ζ_i to the main damage parameter ω_i. Barr and Lee (2003) have recently reviewed a number of softening curves for concrete in tension and have themselves proposed a softening function with two exponential terms. van Mier (1997) has also reviewed these softening functions and highlights the function suggested by Hordijk (1991) which was based upon a wide range of experimental data. However, none of the functions given in the above references satisfies all of the criteria required of the new damage evolution function. The motivation behind changing the function was to improve the numerical performance of the model, and for this purpose a completely continuous curve, which had a smooth transition from undamaged to damaged states and from the pre-peak to the post-peak region, was required. The primary reason for this is that, in the context of a non-linear finite element incremental iterative solution procedure, if there is an abrupt change between states, then numerical integration points can oscillate between these states within the iterations of a single load increment, and in such cases progress towards a converged state may be impeded. The criteria set for finding a suitable damage evolution function were that the function should

(i) have a completely smooth transition between undamaged and damaged states and between pre-peak and post-peak stages,
(ii) be separately scaleable for the pre and post-peak sections,
(iii) be able to be specified in terms of the strain at peak stress and the peak stress
(iv) be asymptotic to the strain parameter axis and not to have a final cut-off point.

Criterion (ii) is important because, up to a certain level of damage which is here taken as that associated with the peak, the damage will remain distributed and thus may be regarded a function of a fixed material strain parameter alone. However, as the loading progresses beyond the peak, strains tend to localise and the apparent local strain becomes dependent upon a characteristic dimension, which can vary between elements. If, as is the case here, the model is implemented using the Bazant-Oh (1983) crack-band approach, this is the characteristic element dimension (w_c).

The function, which is illustrated in Fig. 2 in terms of the fracture stress f_s and the strain parameter ζ, has -as control parameters- the stress at first damage f_{ti}, the associated strain ε_{ti}, the uniaxial strength f_t, the strain at peak stress ε_k and the strain at the effective end of the curve ε_0. The basic function, in which the damage plane subscript has been omitted for clarity, is as follows;

$$f_s = f_{ti} \cdot \text{func}(\zeta) = (1 - \omega(\zeta))E\zeta \tag{13}$$

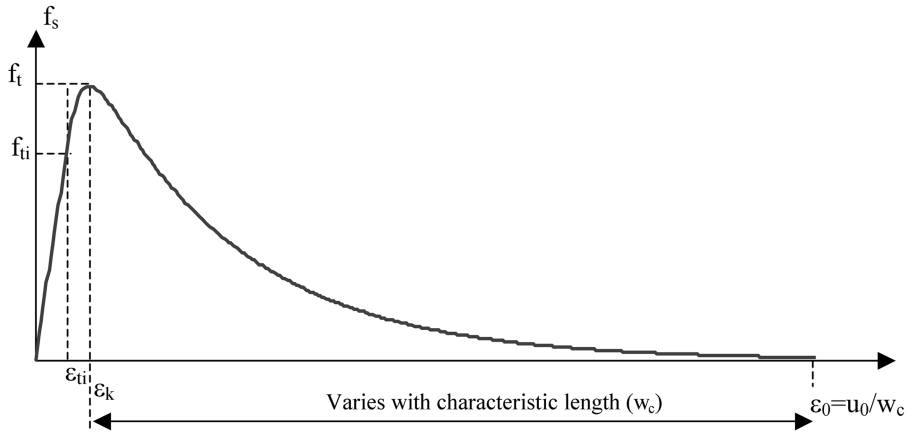

Fig. 2 Damage evolution function

with

$$\omega = 1 - \frac{\varepsilon_{ti}}{\zeta} e^{-c_1 \eta} (a - b e^{-c_1 m \eta} - c e^{-c_1 m p \eta}) \tag{14}$$

The form used to derive the constants is the direct relationship between f_s and ζ, as follows

$$f_s = f_{ti} e^{-c_1 \eta} (a - b e^{-c_1 m \eta} - c e^{-c_1 m p \eta}) \tag{15}$$

in which $\eta = \dfrac{\zeta - \varepsilon_{ti}}{\varepsilon_0 - \varepsilon_{ti}}$

c_1 and p are both assumed to be fixed at 5, although they could be introduced as material parameters. The constants a, b, c and m are determined from the following four conditions;

$$f_s = f_{ti} \quad \text{at} \quad \eta = 0 \tag{16a}$$

$$\frac{\partial f_s}{\partial \zeta} = E \quad \text{at} \quad \eta = 0 \tag{16b}$$

$$f_s = f_t \quad \text{at} \quad \eta = \eta_k \tag{16c}$$

$$\frac{\partial f_s}{\partial \eta} = 0 \quad \text{at} \quad \eta = \eta_k \tag{16d}$$

in which E is Young's modulus and η_k is η at $\zeta = \zeta_k$

Eq. (17), below, may be obtained from Eqs. (16a) and then Eq. (18) by using Eqs. (17) and (16b)

$$a = 1 + b + c \tag{17}$$

$$q = bm + cmp \tag{18}$$

in which $q = \dfrac{\varepsilon_0 - \varepsilon_{ti}}{c_1 \varepsilon_{ti}} + 1$

Using Eqs. (17) and (18) to eliminate a and b, Eqs. (19) and (20) may be derived using conditions (16c) and (16d) respectively;

$$c = \frac{\dfrac{1}{a_t x_k} - 1 - \dfrac{q}{m}(1 - x_k^{\,m})}{1 - x_k^{\,mp} + pxk^{m} - p} \tag{19}$$

$$c = \frac{1 + \dfrac{q}{m}(1 - (1+m)x_k^{\,m})}{p - 1 - (1+m)px_k^{\,m} + (1+mp)x_k^{\,mp}} \tag{20}$$

Equating (19) to (20) and rearranging gives the following equation, in which m is the only unknown

$$\left[\left(\frac{1}{a_t x_k} - 1 - \frac{q}{m}1 - x_k^{\,m}\right)\right)(p - 1 - p(1+m)x_k^{\,m} + (1+pm)x_k^{\,pm})\Big] - \left[\left(1 + \frac{q}{m}1 - (1+m)x_k^{\,m}\right)\right)(1 - x_k^{\,mp} - p + px_k^{\,m})\Big] = 0 \tag{21}$$

in which

$$x_k = e^{-c_t \eta_k} \text{ and } a_t = \frac{f_{ti}}{f_t}$$

Eq. (21) is highly non-linear and not readily amenable to an analytical solution. Since the aim of this section is the development of an equation suitable for finite element applications, it would be possible to implement a numerical solution of Eq. (21) based on, for example, a combination of bisection and Newton algorithms (Press, *et al.* 1992). However, it proved possible to find an approximate solution for Eq. (21) that proved more attractive for numerical implementation. The value of m varies with x_k and q, but both of these are functions of a strain parameter ratio r_ε, defined below, and thus it is possible to derive a relationship between m and r_ε

$$r_\varepsilon = \frac{\varepsilon_0 - \varepsilon_{ti}}{\varepsilon_{ti}} \tag{22}$$

It was found that the actual function for m is closely fitted by a function of the form

$$m = z_1 + z_2 r_\varepsilon + z_3 r_\varepsilon^{\,d} \tag{23}$$

in which d is fixed as 1.005 and the constants z_i are evaluated to minimise the error between the approximate and actual root functions for m.

The z coefficients that minimise the error between the actual and approximate values of m for a range of range of $(\zeta_k / \varepsilon_t)$ ratios are given in Table 1, for an a_t value of 0.75. It is noted that that $\varepsilon_t = f_t/E$.

Table 1 Coefficients for m root function

$(\zeta_k / \varepsilon_t)$	z_1	z_2	z_3
1.2	0.209165281613623	-80.9498899028202	80.2928557910858
1.3	0.223098944982796	-67.0625617052971	66.4302094339053
1.4	-0.012843219153829	-57.1695517518859	56.5717813830593
1.5	-7.2167464803493	-39.622646207189	39.3906325087707
1.6	-4.44312469371335	-38.8109320569211	38.4516691355379
1.7	-1.66691145999311	-39.7346144314323	39.2268743525994

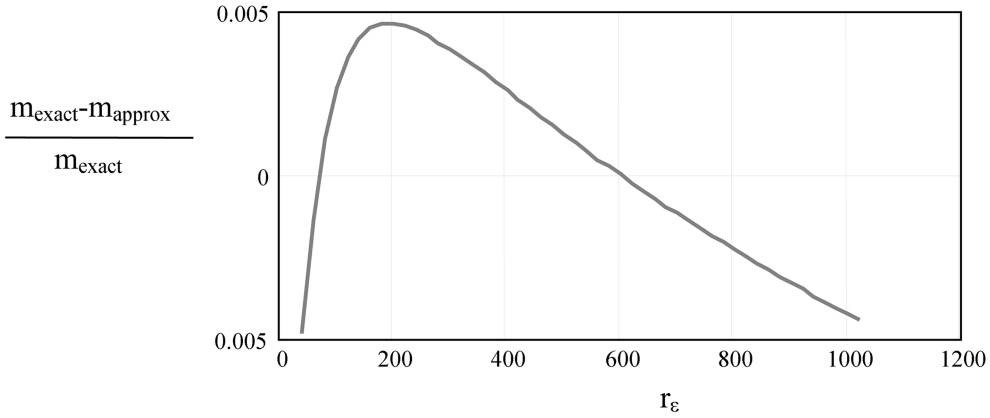

Fig. 3 Normalised error in m

The maximum normalised error in m for a range of r_ε from 20 to 1000 is 0.5%, and with this level of error, m has a negligible effect on the final equation. The normalised error in m, for the case of $(\zeta_k / \varepsilon_t) = 1.3$, is shown in Fig. 2. The 'exact' values of m were computed using the non-linear equation solution facility within the program Mathcad.

The use of the new function in a finite element code involves evaluating ε_0 from the element characteristic length, fracture energy parameter G_F and a standard softening curve Eq. (24), as illustrated in Eq. (25). Then m is obtained from Eq. (23), c from Eq. (19), b from Eq. (18) and a from Eq. (17). Once a first estimate of the actual softening curve (15) is available, ε_0 may be re-evaluated based on the actual softening curve and m, c, b, a also re-evaluated. One iteration of this process is adequate.

$$f_s = f_t e^{-c_1 \eta} \tag{24}$$

$$\varepsilon_{0\_first\_estimate} = \frac{c_1 G_F}{w_c f_t} + \varepsilon_t \tag{25}$$

4. Contact proportion function H_f

As shown in Eq. (1), the local stress in the damaged component is a function of H_f, which reduces with the increasing strain opening parameter e_g (see Fig. 1). The purpose of H_f is to simulate the observed behaviour that the wider a crack the less is the shear stress that can be develop with increasing shear strain. H_f becomes effectively zero when the opening strain reaches a value at which no further shear contact is possible. This is taken as a multiple (m_{ful}) of the strain value at the end of the softening curve i.e., $m_{ful}\ \varepsilon_0$.

The H_f function given in Jefferson (2003a) was developed using the data of Walraven and Reinhardt (1981). However, it has been found that when simulating shear-normal experiments which used specimens made from concrete with relatively small coarse aggregate, such as in the tests of Hassenzadeh (1991), the original function overestimated the build up of post crack shear and normal stresses at small openings. Thus, a modified function has been adopted which includes a parameter associated with the early stages of opening, termed m_{hi}. The basic function shown in the { } brackets in Eq. (26) is multiplied by a constant $H_m = 0.995$, the reason for which was explained in Jefferson (2003a) and a smooth but rapid embedment function $H_g(g)$ also defined in the preceding reference. The basic function comprises two phases, the first governed by the strain ratio η_0, which controls the early reduction phase and the second, governed by η_1, which controls the later stages of reduction. The third term provides a correction to give a zero initial slope and makes the curve continuous at e_{bg}, which defines the start of contact reduction. Typically the material parameters m_{hi} and m_{ful} are in the range 0.3 to 0.5 and 5 to 20 respectively. The basic H_f function is illustrated in Fig. 4.

$$H_f = H_m \quad \text{if} \quad e_g < \varepsilon_{bg}$$

$$H_f = H_m H_g(g)\left\{\frac{1}{1-f_h}\left(r_f e^{-\rho_{f0}\eta_0^2} + (1-r_f)e^{-\rho_{f1}\left(\frac{e_g-\varepsilon_t}{m_{ful}\varepsilon_0}\right)} - f_h e^{-\rho_{f0}\eta_0^2}\right)\right\} \tag{26}$$

in which

$$f_h = (1-r_f)\frac{\rho_{f_1} m_{hi}}{\rho_{f_0} m_{hi}}, \quad H_g(g) = \left(1 - e^{-c_g \frac{g}{e_g + 2\varepsilon_t}}\right), \quad \eta_0 = \frac{e_g - \varepsilon_{bg}}{m_{hi}\varepsilon_0}, \quad \eta_1 = \left(\frac{e_g - \varepsilon_{bg}}{m_{ful}\varepsilon_0}\right) \& e_{bg} = 1.1\varepsilon_t$$

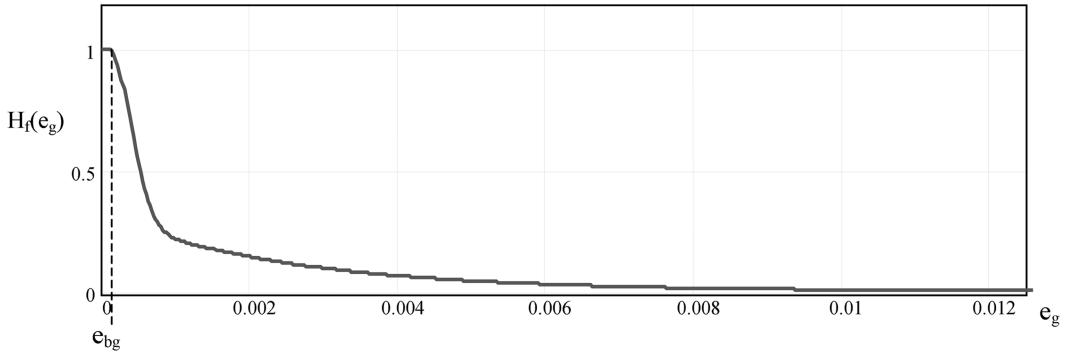

Fig. 4 Contact proportion function

where $r_f = 0.7$, $\rho_{f0} = 10$, $\rho_{f2} = 5$ and $c_g = 3$

5. Implications of new damage evolution function on stress mapping/tangent matrix algorithm

The first damage plane at any numerical integration point occurs when the major principal stress exceeds the initiation stress f_{ti}. The same criterion can be used for the formation of a second damage plane when the damage evolution function only has a post-peak section, as in Jefferson (2003a), and therefore $f_{ti} = f_t$. However, this criterion presents a problem for the formation of the second and subsequent planes when a permanent damage plane is already present, if the damage evolution function has a pre-peak. This is because the major principal stress may be in (or close to) the first plane direction, whilst a second plane may be required to form. Assuming that a lower limit is applied to the directional proximity of adjacent planes, then the situation can arise when the normal stress on a would-be second plane exceeds the formation limit but the major principal stress is too close to the first plane direction for the plane to form. An alternative approach, when the major principal stress exceeds f_{ti}, but the associated principal direction is too close to the first plane, is to form a second plane when the damage function on the nearest permissible plane to the first is exceeded. The same approach can be applied to subsequent planes. This however creates a further problem in that the consistent algorithm described in Jefferson (2003b) requires damage planes to form in principal directions, since the rate of change of the principal directions is taken into account in the consistent tangent matrix.

If $\boldsymbol{\sigma}_I$ is the stress tensor upon which the crack direction is based, then the derivative of the stress transformation matrix with respect to $\boldsymbol{\sigma}_I$ is required i.e., $\partial \mathbf{N}_i / \partial \boldsymbol{\sigma}_I$. This is calculated using the chain differentiation rule, such that if a new plane is associated with the major principal value σ_1 of $\boldsymbol{\sigma}_I$, and the normal and shear directions are given by the unit vectors $\mathbf{r}_d$, $\mathbf{s}_d$ and $\mathbf{t}_d$, then $\partial \mathbf{N}_i / \partial \boldsymbol{\sigma}_I$ is given by

$$\frac{\partial \mathbf{N}_i}{\partial \boldsymbol{\sigma}_I} = \frac{\partial \mathbf{N}_i}{\partial r_d}\frac{\partial r_d}{\partial \boldsymbol{\sigma}_I} + \frac{\partial \mathbf{N}_i}{\partial s_d}\frac{\partial s_d}{\partial \boldsymbol{\sigma}_I} + \frac{\partial \mathbf{N}_i}{\partial t_d}\frac{\partial t_d}{\partial \boldsymbol{\sigma}_I} \tag{27}$$

When the alternative criterion, of the damage function being greater than zero on the nearest plane to the existing and the major principal stress planes, is used the above no longer applies. A scheme to deal with this case will be explained for a case of the formation of a second damage plane with one existing plane having the normal $\mathbf{r}_e$. The criterion is applied that a new plane can not form within an angle of α_p from an existing plane. If the major principal direction of the stress state under consideration ($\mathbf{r}_\sigma$) is within α_p of $\mathbf{r}_e$ i.e., $\mathbf{r}_e \cdot \mathbf{r}_\sigma > \cos(\alpha_p)$, then the damage function is checked on a plane which has a normal which lies in the same plane as $\mathbf{r}_e$ and $\mathbf{r}_\sigma$ but is at an angle of α_p to $\mathbf{r}_e$. The unit vector in the plane of $\mathbf{r}_e$ and $\mathbf{r}_\sigma$ that is orthogonal to $\mathbf{r}_e$ is denoted $\mathbf{r}_0$ and may be calculated as follows

$$\mathbf{r}_0 = \frac{\mathbf{r}_e \times \mathbf{r}_\sigma}{|\mathbf{r}_e \times \mathbf{r}_\sigma|} \times \mathbf{r}_e \tag{28}$$

The normal to the required plane ($\mathbf{r}_n$) at an angle α_p to $\mathbf{r}_e$ is then given by

$$\mathbf{r}_n = \cos(\alpha_p)\mathbf{r}_e + \sin(\alpha_p)\mathbf{r}_0 \tag{29}$$

In this case Eq. (27) still applies but $\mathbf{r}_n$ replaces $\mathbf{r}_d$, and both $\mathbf{s}_d$ and $\mathbf{t}_d$ are constructed from the new direction $\mathbf{r}_n$. The differential with respect to the principal stress is still relevant but is now given by

$$\frac{\partial \mathbf{r}_n}{\partial \sigma_1} = \sin(\alpha_p)\mathbf{r}_0 \frac{\partial \mathbf{r}_0}{\partial \mathbf{r}_\sigma}\frac{\partial \mathbf{r}_\sigma}{\partial \sigma_1} \tag{30}$$

When two or three planes form in one increment, the above problem does not arise because the directions are orthogonal to each other since they are all based on principal directions.

6. Experimental examples

All of the example analyses presented here are taken from the PhD Thesis of Brokenshire (1995) (Barr and Brokenshire, 1996), however, the full details of the tests have not been published elsewhere, hence relevant experimental details will be presented in the following, prior to descriptions of the analyses.

6.1. Description of torsion fracture tests due to Brokenshire

The primary aim of the work of Barr and Brokenshire (1996) was the development of a torsion fracture test suitable for concrete cores taken from existing structures. In order to provide comparisons with the standard RILEM test method (RILEM TC50 1985), which uses notched beam specimens, a series of different tests were conducted on each batch of concrete, which included notched RILEM type beams, notched prismatic specimens under torsion and notched cylindrical specimens also under torsion. In addition, a series of un-notched cylindrical beams were tested in

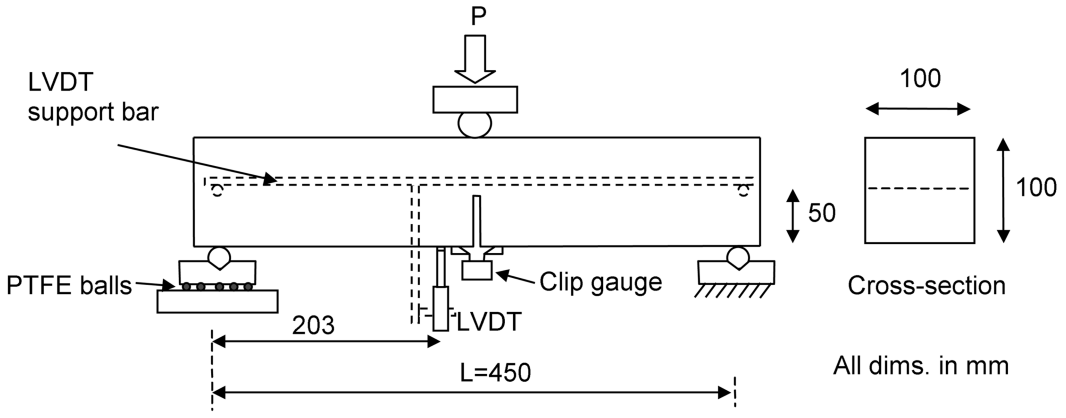

Fig. 5 Testing arrangement for notched beam tests

torsion to establish the elastic properties and torsional shear strength. Two types of aggregate were used in the work, namely locally supplied crushed limestone and gravel with rounded particles, both with maximum size of 10mm. Three mixes were used with nominal strengths of 40, 70 and 100 MPa (denoted C40, C70 and C100 respectively) and in addition, a mortar mix with a nominal strength of 70MPa was also used. Here, only specimens made with the C40 mix with 10mm crushed limestone aggregate will be considered. This mix used ordinary Portland cement and locally supplied sea-dredged sand. The mix proportions were as follows; cement to sand to coarse aggregate proportions of 1:2:2.5 and water cement ratio of 0.55 (all by weight). All specimens were stored in water until 24 hours before testing, at which point they were removed and, if relevant, notches cut.

The notched beam tests used specimens of a different length from that suggested in the RILEM paper (RILEM TC50 1985), but otherwise these tests complied with the method. The specimens used were 100 mm × 100 mm in cross-section by 500 mm in length. The span (L) of the beams was 450mm. The notched beam testing arrangement is shown in Fig. 5, in which the loading rate is controlled via feedback from a clip gauge at the notch mouth. The displacement was measured at a location 0.05L from the centreline on the underside of the beam, with the displacement transducer mounted on a frame supported from the beam at two points directly above the supports. Tests were performed with two notch depths of 0.3D and 0.5D, although only the 0.5D cases will be considered here, where D is the beam depth. The reason for including these tests is that they provide an acceptable benchmark for the evaluation of the fracture parameters. It was found that the fracture energies evaluated from some of the notched torsion tests varied from those of the beam test, and so the fracture energies used in the analyses are based on notched beam values. It has in fact been known for some time that measured fracture energies do vary with the size and geometry of specimens as well as with the notch depth (Guinea, *et al.* 1992), and a proposal has recently been made for the evaluation of a size and geometry independent G_F value, i.e., a true fracture energy parameter (Abdalla and Karihaloo, 2003).

Turning attention to the notched torsion tests; the rationale behind introducing a notch at an angle of 45° to the axis of the specimen was to encourage a mode I crack to form in a direction normal to

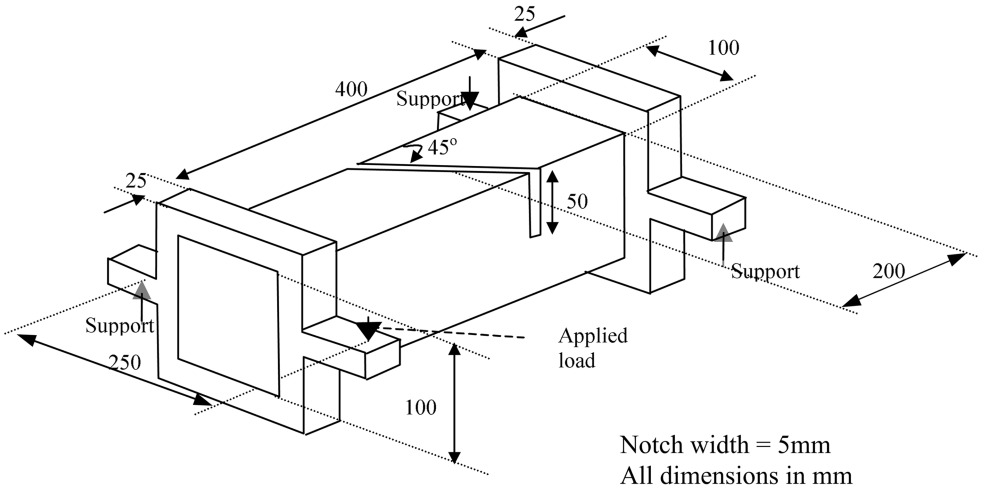

Fig. 6 Testing arrangement for notched prismatic torsion test

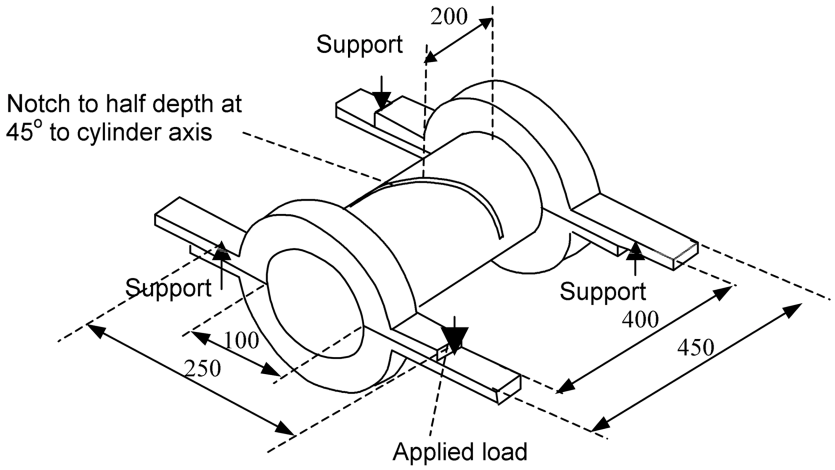

Fig. 7 Testing arrangement for notched cylindrical torsion test

the major principal stress of an un-notched elastic cylindrical specimen. Although the stress distribution in the notched specimens departs substantially from that of an un-notched specimen, the tests did show that cracks opened from the edge of the notches, although as may be seen from the photograph of the failed specimen, the failure surface in the prismatic sections was curved and did not coincide exactly with that of the notch. It did however prove possible to evaluate the fracture energy parameter G_F by considering the total work done in forming the crack. Also, by using feedback from a clip gauge, mounted on knife-edges at the notch mouth, the full pre and post-peak response of the specimens were captured. Measurements taken included the load, the displacement at the point the load was applied to the arm of the loading collar, the notch mouth opening displacement, called hereafter the Crack Mouth Opening Displacement (CMOD), and a tangential displacement measured from a frame attached to the concrete specimens. In a later test series, which was intended to further explore failure modes, both opening and sliding displacements were measured at the notch mouth. Specimens with notch depths of 0.3D and 0.5D were tested but here only specimens with 0.5D cases will be considered for finite element analysis.

In all torsion tests the load was applied through a steel ball mounted on a shaft at the end of the loading ram, which was seated in a hemi-spherical recess in one arm of the loading collar. The three supports were all steel rods, with those acting upwards having rounded ends seated in the arm of the end collar, whilst the restraining support was a threaded bar with a nut which retained the arm of the loading collar. The testing arrangements for both the prismatic and cylindrical torsion tests may be seen in the photographs in Plates 1 and 2 and are also illustrated in Figs. 6 and 7. In the prismatic torsion tests, the end collars were bolted onto the specimen with hardboard packing strips being placed between the specimens and collars. For the cylindrical specimens, grooves parallel with the cylinder axis were cut with a hand grinder at the ends and then the collars, which had serrated inner surfaces, were glued to the specimens and later (once the glued had set) secured by bolting. All notches were nominally 5 mm in width and cut with a frame mounted masonry saw.

In the test programme, each test (i.e., specimen with same geometry, notch and mix) was conducted four times in each test series. Also, for each batch of concrete, four cubes and four cylinder splitting tests were tested. The results provided mean and Coefficient of Variation (CoV)

Table 2 Concrete properties from experimental programme

Test Series / Batch	[1] E kN/mm^2	f_{cu} N/mm^2 (CoV %)	f_{spl} N/mm^2 (CoV %)	[2] G_F (N/m) (CoV %)
Series II Prismatic torsion & notched beams 2.1	34.9	40.3 (2.4)	2.83 (4.2)	73.5 (5.8)
Series II Cylindrical torsion & notched beams 2.2	-	38.6 (2.1)	3.43 (13.5)	83.9 (9.1)
Series III prismatic torsion	-	40.2 (3.4)	3.08 (10)	-
Series III Cylindrical torsion	-	43.9 (0.6)	3.08 (7.9)	-

1. E not measured separately for each batch. 2. G_F from beam tests
f_{cu} = cube strength, f_{cyl} = cylinder splitting strength

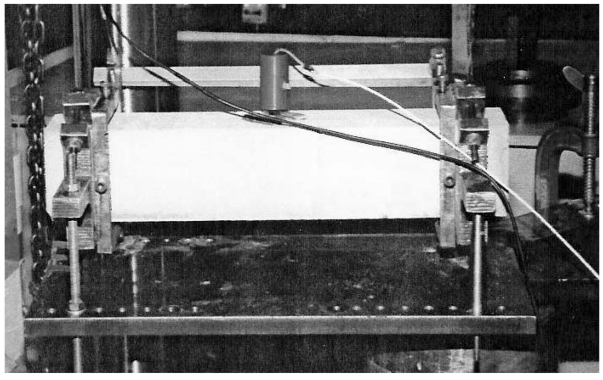

Plate 1 Notched prismatic torsion test (After Brokenshire 1995)

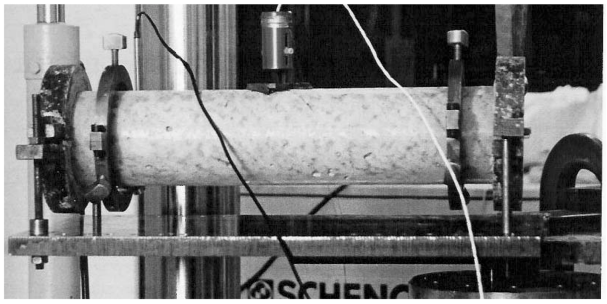

Plate 2 Notched cylindrical torsion test (After Brokenshire 1995)

values for each parameter. The test sets considered here were carried out separately in three different series. The first being a test development series (I), in which the restrained length was varied in addition to the other parameters discussed, the second (II), a so-called G_F test series, aimed at evaluating the differences between the G_F values from the torsion and notched beam tests and a final series (III) in which the sliding displacement was measured to test the degree to which

the tests were Mode I. Representative response graphs are available for each series although these are not available for all of the tests conducted. Here the results from test series II and III will be used, these being considered the most reliable. For test series II, representative displacement and CMOD opening displacement responses are available and for test series III, the CMOD opening and sliding displacements are available, thus two experimental lines appear only on the load-CMOD opening graphs. For test series II, notched prismatic beam specimens were also made from each batch of concrete. Thus, fracture energy (G_F) results from the notched beams are available separately for the mixes used for the prismatic and cylindrical torsion test specimens of test series II. However, beam tests were not conducted for test series III. The results from the control specimens and three-point fracture beam tests for the tests considered for analysis are given in Table 2.

The efficaciousness, or otherwise, of the tests, with respect to the original aim of the experimental programme, is not the concern of the present contribution; however, it is noted that there was reasonable agreement between the G_F values from the notched torsion prismatic tests and the benchmark three point bend tests, but the G_F values evaluated from the notched cylindrical specimens were somewhat lower than those from the other two tests for the same mixes. Also, the measurements and shape of the failure surface showed that cracks in the prismatic specimens did not form in a single mode I fashion, at least with respect to the original notch plane. However, for the present purpose of validating a three dimensional numerical concrete model, these carefully conducted experiments are considered to provide excellent benchmark examples.

The results from the tests in terms of load CMOD and load displacement responses are shown along with the results from the analyses in the following section.

7. Finite element analyses

The tests discussed in the previous section have been considered in finite element analyses. All the tests considered in this section had the same design mix although, as may be seen in Table 2,

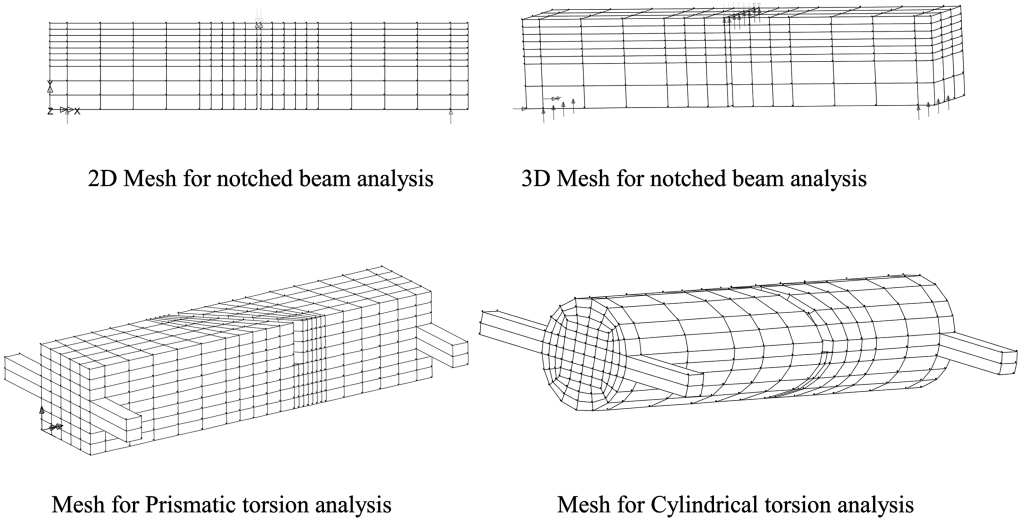

Fig. 8 Finite element meshes

the results of the different batches varied a little. The approach taken in the following series of analyses is to use a single set of material properties for all cases. The values used are shown in Table 3. It is assumed that the uniaxial compression strength $f_c = 0.8f_{cu}$ and the tensile strength is $f_t = 0.8f_{cyl}$.

Table 3 Properties used for analyses

E kN/mm^2	n	f'_c N/mm^2	f_t N/mm^2	ε_c	G_F N/mm	m_g	m_{hi}	m_{ful}
35	0.2	32	2.3	0.0023	0.08	0.5	0.5	5

The analyses undertaken include a two-dimensional and a three-dimensional analysis of the notched beam specimen, a three-dimensional analysis of the notched prismatic torsion specimen and a three-dimensional analysis of the notched cylindrical torsion specimen.

The analyses were undertaken using the finite element program LUSAS (LUSAS, 2003) with the amended Craft model (as described above) implemented via the material model interface. All meshes were formed from bilinear (2D) or trilinear (3D) elements and are shown in Fig. 8. The characteristic length is computed at each element Gauss point using the square root or cube root of the element Jacobian for two and three dimensional elements respectively (the root value obtained is multiplied by two since the local element coordinate system varies from -1 to +1).

The meshes for the torsion specimens include the loading arms but not the collars. To allow for this the end elements are given a higher stiffness ($5*E_{steel}$). It is noted that in the actual torsion tests the response at the points the load were applied to the loading arm exhibited snapback behaviour. Such behaviour can be simulated numerically using an arc length method e.g., (Crisfield, 1981) however, in the present analyses the results did not exhibit snap-back because the stiffness of the end sections and arms were increased, and this allowed a prescribed displacement loading procedure to be used. The present approach is considered reasonable since the distribution of stresses in the specimens in the region adjacent to the collars should be very similar to that in the experiments. It is noted that the loads in the analyses were applied in the same locations, relative to the specimens, as those shown in Figs. 6 and 7 for the actual tests.

The convergence tolerance used for the residual force and displacement norms were both 0.001. The solutions all employed an automatic step selection procedure in which the displacement or load

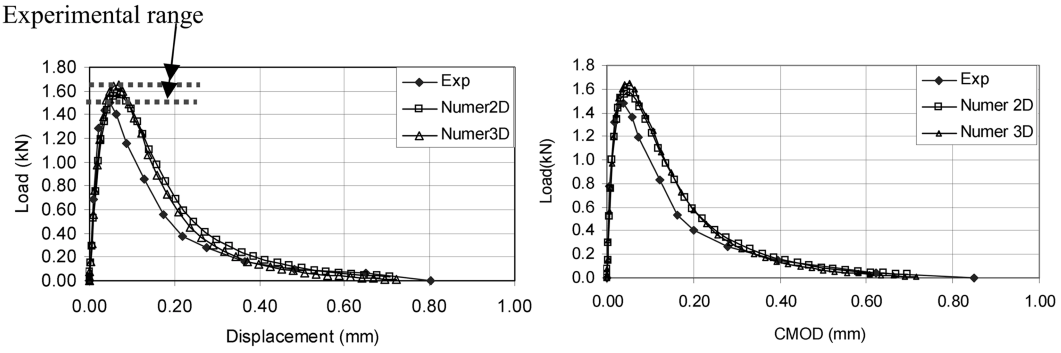

Fig. 9 Notched beam response

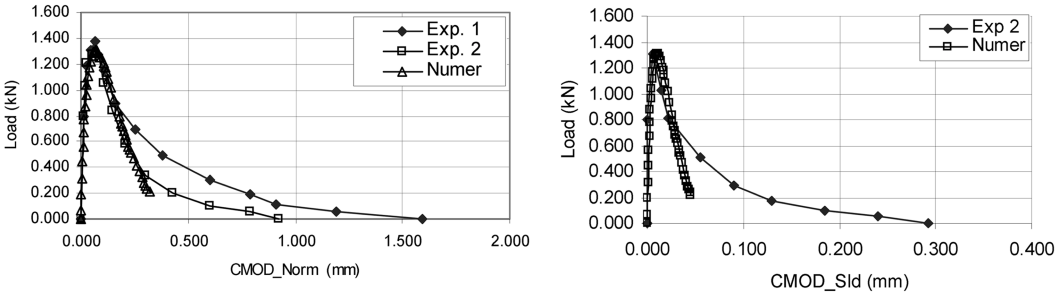

Fig. 10 Load CMOD responses for prismatic torsion tests

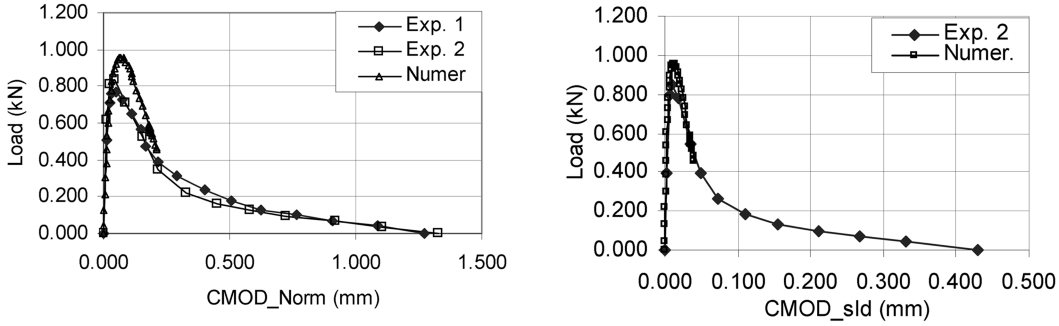

Fig. 11 Load CMOD responses for cylindrical torsion tests

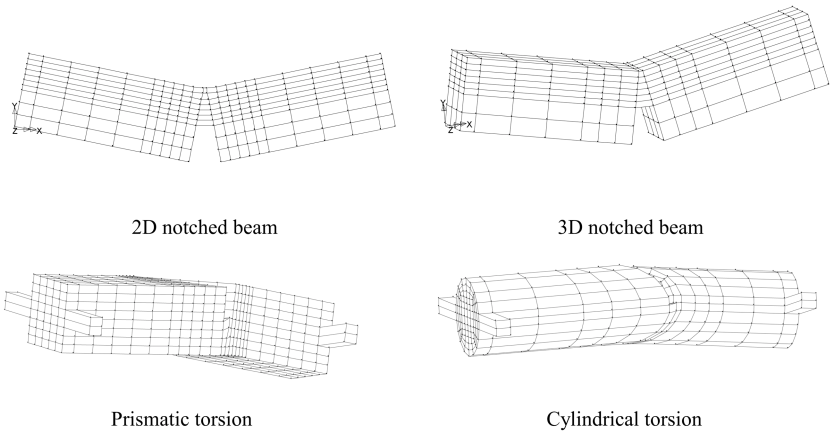

Fig. 12 Deformed meshes at last analysis step. Displacement magnification factor = 20

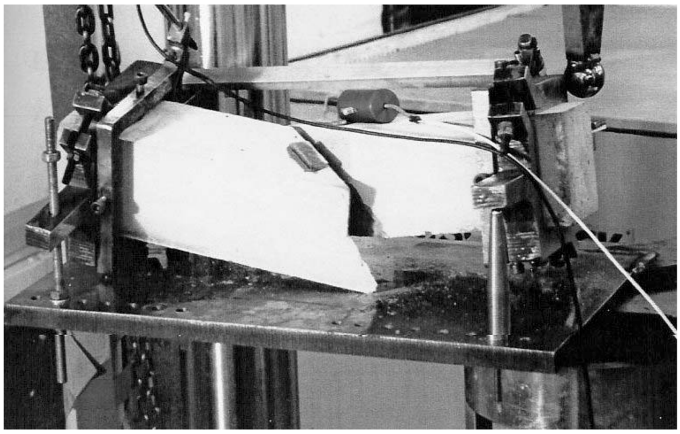

Plate 3 Prismatic torsion test after failure (After Brokenshire 1995)

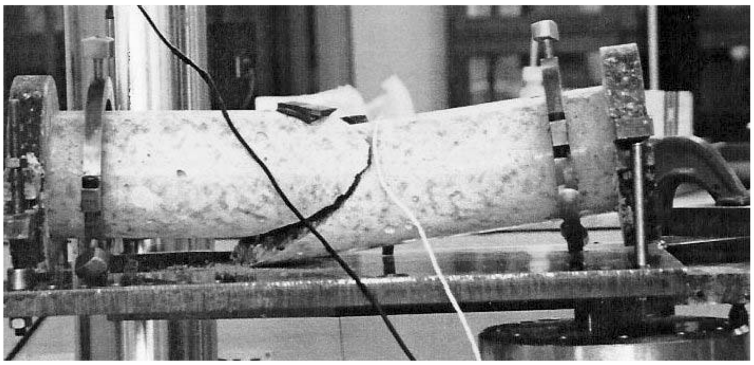

Plate 4 Cylindrical torsion test after failure (After Brokenshire 1995)

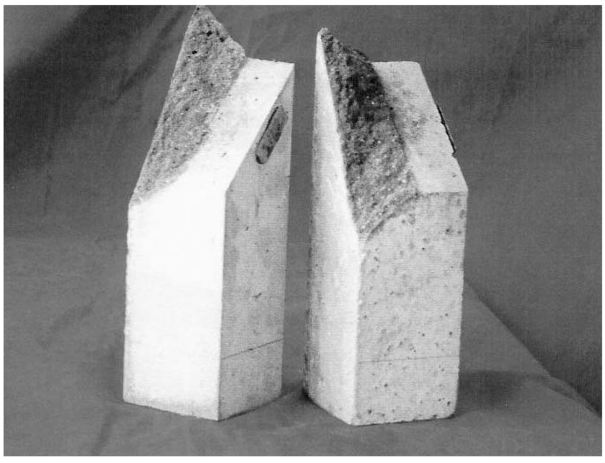

Plate 5 Prismatic torsion specimen after failure (After Brokenshire 1995)

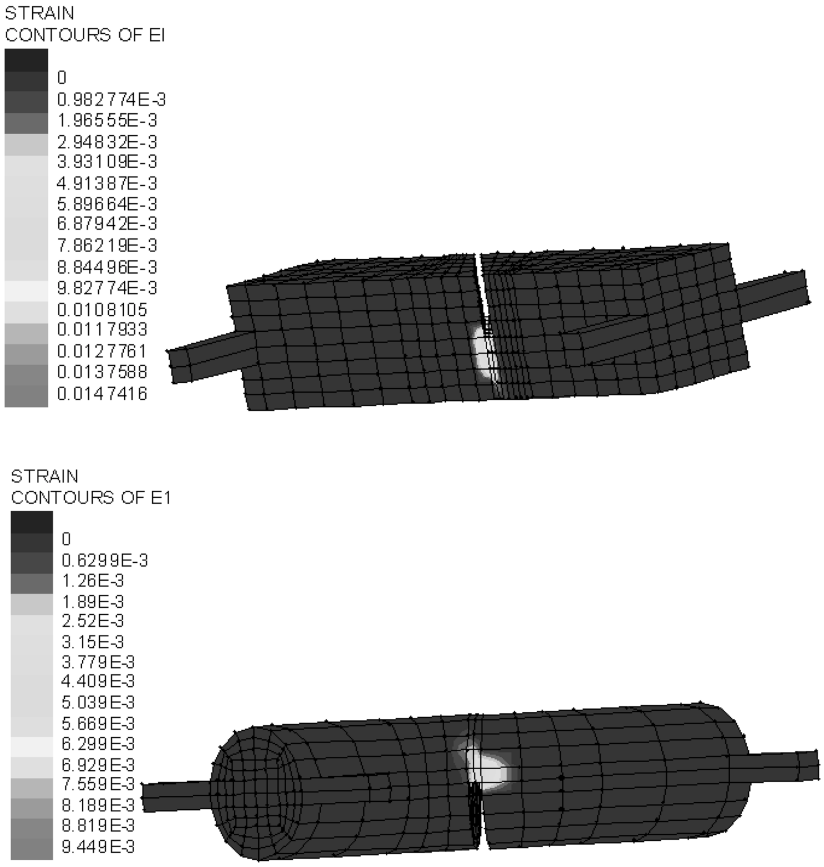

Fig. 13 Major principal strain at last analysis step for torsion examples

increment is adjusted according to the number of iterations taken to achieve convergence in the previous step. The standard number of target iterations was set to 4 and the maximum number of iterations permitted before automatic step reduction was set between 6 and 8. The total number of steps used for all solutions was in the range of 40 to 50.

The numerical and experimental responses for all three sets of analyses are shown in Figs. 9 to 11. It is noted that the displacement for the notched beam test is at the location of the LVDT shown in Fig. 5.

Notched beam tests do not represent a particular challenge for numerical simulation since they do not, in general, involve changes in crack directions since they tend to follow pure mode I opening behaviour. The numerical results here do slightly overestimate the peak load, relative to the representative curve shown, however, the results are very close to the upper bound of the experimental peak load range, which is shown on the graph. The analysis is able to capture the full tail of the response curves and proceeded with no problems.

The torsion cases proved more difficult to analyse and in these analyses the tail of the numerical response curves do not closely match those of the experimental curves. However, the peak loads and load-$CMOD_{norm}$ were captured quite well until the start of the tail, with the numerical and

experimental results being closer for the prismatic case than for the circular case. These analyses of the notched torsion tests are considered a partial success. The authors had not previously been able to capture the post-peak response to any significant degree with other material models using the smeared crack approach and were unable to achieve the numerical predictions to the extent shown here without the model developments referred to in Sections 3 to 5 of this paper. It is recognised that the meshes are relatively coarse, and perhaps these are not fine enough to capture the end stages of the fracture process in the torsion tests. The authors are therefore currently investigating the use of non-local strain measures and considerably finer meshes in an attempt to better capture the tail of the experimental response.

8. Conclusions

The paper has provided a description of the recently developed Craft plastic-damage-contact model for concrete and has included two particular new developments, a smooth pre-peak/post peak softening curve that provides a completely smooth transition from the undamaged to the damaged state, and an improved contact reduction function. The implications of implementing the smooth pre-peak/post-peak softening curve with a consistent stress recovery/tangent stiffness algorithm have been discussed and necessary amendments to the existing algorithm have been described. The model was used for all simulations presented in this paper and the model developments allowed the simulation of the torsion fracture tests to a degree which was not found possible without these amendments. It is therefore concluded that the developments provide useful enhancements to the model.

The paper also has presented details of a series of fracture tests on notched specimens, which included three-point bend, prismatic and cylindrical torsion tests. These tests were presented primarily to provide three-dimensional benchmarks for validating the present numerical model. The model was able to represent the notched beam test throughout the response range reasonably well, whereas the numerical simulations were not able to capture all latter stages of the behaviour of the torsion tests, although the peak load and early post-peak responses were captured reasonably. The conclusions from the series of simulations were that the validations were partially successful. Further work on this is being undertaken in which non-local strains with finer meshes are being used to attempt to better capture the tail of the experimental response.

Finally it is concluded that the torsion tests described provide useful three-dimensional examples for validating numerical models for concrete.

Acknowledgements

The authors would like to acknowledge support from the U.K. Engineering and Science Research Council grant GR/S05168 and FEA Ltd. for their help and support over a number of years in the development of finite element material models. Furthermore, the authors acknowledge the experimental work of David Brokenshire which has been considered for the analyses presented in this paper.

References

Abdalla, H. M. and Karihaloo, B. L. (2003), "Determination of size independent specific fracture energy of concrete from three-point bend and wedge splitting tests", *Mag. Conc. Res.*, **55**, 133-141.

Barr, B. I. G. and Brokenshire, D. R. (1996), Torsion fracture tests, *BRE Digest*.

Barr, B. I. G. and Lee, M. K. (2003), "Modelling the strain-softening behaviour of plain concrete using a double-exponential model", *Mag. Conc. Res.*, **55**(4).

Bažant, Z. P. and Oh, B. H. (1983), "Crack band theory for fracture in concrete", *Mater. Struct.* **16**, 155-177.

Bažant, Z. P., Caner, F. C., Carol, I., Adley, M. D. and Akers, S. A. (2000), "Micro-plane model M4 for concrete. I Formulation with work conjugate deviatoric stress", *J. Eng. Mech., ASCE*, **126**(9), 944-953.

Brokenshire, D. R. (1996), "A study of torsion fracture tests", Ph. D. Thesis, Cardiff University, U.K.

Crisfield, M. A. (1981), "A fast incremental/iterative solution procedure that handles snap-through", *Comp. Struct.* **13**, 55-62.

de Borst, R. (2003), "Numerical aspects of cohesive zone models", *Eng. Frac. Mech.*, **70**(14), 1743-1757.

de Borst, R. and Nauta, P. (1985), "Non-orthogonal cracks in a smeared finite element model", *Eng. Comput.* **2**, 35-46.

Este, G. and Willam, K. (1994), "Fracture energy formulation for inelastic behaviour of plain concrete", *J. Eng. Mech. ASCE*, **120**(9), 1983-2011.

Grassl, P., Lundgren, K. and Gylltoft, K. (2002), "Concrete in compression: a plasticity theory with a novel hardening law", *Int. J. Solids Struct.,* **39**, 5205-5223.

Gopalaratnam, V. S. and Shah, S. P. (1985), "Softening response of plain concrete in direct tension", *ACI J.* **82**(3), 310-323.

Guinea, G., Planas, J. and Elices, M. (1992), "Measurement of fracture energies using three-point bend tests : Part 1. Influence of experimental procedures", *Mater. Struct.* **25**, 212-218.

Hassanzadeh, M. (1991), "Behaviour of fracture process zones in concrete influenced by simultaneously applied normal and shear displacements", Ph. D. Thesis, Lund Institute of Technology, Sweden.

Hordijk, D. A. (1991), "Local approach to fatigue of concrete", Ph. D. Thesis Delft University of Technology, The Netherlands.

Jefferson, A. D. (2003a), "Craft, a plastic-damage-contact model for concrete I. Model theory and thermodynamics", *Int. J. Solids Struct.,* **40**(22) 5973-5999.

Jefferson, A. D. (2003b), "Craft, a plastic-damage-contact model for concrete II. Model implementation with implicit return mapping algorithm and consistent tangent matrix", *Int. J. Solids Struct.,* **40**(22), 6001-6022.

Jirasek, M and Zimmermann, T. (1998), "Rotating crack model with transition to scalar damage", *ASCE J. Engng Mech.*, **124**(3), 277-284.

Jirasek, M and Zimmermann, T. (2001), "Embedded crack model: Part 1 Basic formulation, Part 2: Combination with smeared cracks", *Int. J. Num. Meth. Eng.,* **50**, 1269-1305.

Krajcinovic, D. (1996), *Damage Mechanics*, Elsevier.

Lubiner, J., Oliver, J., Oller, S. and Onate, E. (1989), "A plastic-damage model for concrete", *Int. J. Solids Struct.* **25**(3), 299-326.

Luccioni, B. and Oller, S. (2003), "A directional damage model", *Comput. Meth. Appl. Mech. Eng.*, **192**(9-10), 1119-1145.

LUSAS (2003), *User Reference Manual*, FEA Ltd. Kingston Upon Thames London.

Meschke, G., Lackner, R. and Mang, H. A. (1998), "An anisotropic elastoplastic-damage model for plain concrete", *Int. J. Num. Meth. Eng.* **42**, 703-727.

Moes, N. and Belytschko, T. (2002), "Extended finite element method for crack growth", *Eng. Fract. Mech.*, **69**, 813-833.

Mosler, J. and Meschke, G. (2003), "3D modelling of strong discontinuities in elastoplastic solids: fixed and rotating localisation formulations", *Int. J. Num. Meth. Eng.*, **57**, 1553-1576.

Oliver, J., Huespe, A. E., Pulido, M. D. G. and Chaves, E. (2002), "From continuum mechanics to fracture mechanics: the strong discontinuity approach", *Eng. Fract. Mech.*, **69**, 113-136.

Oliver, J., Huespe, A. E. and Samaniego, E. (2003), "A study on finite elements for capturing strong discontinuities." *Int. J. Num. Meth. Engng*, **56**, 2135-2161.

Ortiz, M. (1985), "A constitutive theory for the inelastic behaviour of concrete", *Mechanics of Materials*, **4**, 67-93.
Owen, D. R. J., Figueriras, J. A. and Damjanic, F. (1983), "Finite element analysis of reinforced and prestressed concrete structures including thermal loading", *Comput. Methods Appl. Mech. Eng.*, **41**, 323-366.
Ozbolt, J. and Reinhardt, H. W. (2002), "Numerical study of mixed-mode fracture in concrete", *Int. J. Fract.*, **118**(2), 145-161.
Press, W. H., Teukolsky, S. A., Vettering, W. T. and Flannery, B. P. (1992), *Numerical Recipes*, Cambridge University Press.
RILEM Technical Committee 50-FMC (1985), "Determination of the fracture energy of mortar and concrete by means of three-point bend tests on notched beams", *Mat. Struct.,* **18**(106) 285-290.
Rots, J. G. (1988), "Computational modeling of concrete fracture", Ph. D. Thesis, Delft University of Technology, The Netherlands.
Walraven, J. C. and Reinhardt, H. W. (1981), "Theory and experiments on the mechanical behaviour of cracks in plain and reinforced concrete subjected to shear loading", *Heron* **26**(1A), Delft, The Netherlands.
Wells, G. N. and Sluys, L. J. (2001), "A new method for modelling cohesive cracks using finite elements", *Int. J. Num. Meth. Eng.*, **50**, 2667-2682.
Willam, K. and Warnke, E. (1975), "Constitutive models for triaxial behavior of concrete", *Proc. Int. Assoc. Bridge Struct. Engrg*, Report 19, Zurich, Switzerland, 1-30.
van Mier, J. G. M. (1997), *Fracture Processes of Concrete,* CRC Press.

CC